

Observation of multiple ionization pathways for OCS in an intense laser field resolved by three dimensional covariance mapping and visualized by hierarchical ionization topology.

W. A. Bryan* and W. R. Newell

Department of Physics and Astronomy, University College London, Gower Street, London WC1E 6BT, UK

J. H. Sanderson

Department of Physics, University of Waterloo, Waterloo, Ontario, Canada N2L 3G1

A. J. Langley

Central Laser Facility, Rutherford Appleton Laboratory, Chilton, Didcot, Oxon OX11 0QX, UK

(Dated: October 2, 2018)

The two- and three-body Coulomb explosion of carbonyl sulfide (OCS) by 790 nm, 50 fs laser pulses focussed to $\approx 10^{16}$ Wcm $^{-2}$ has been investigated by three-dimensional covariance mapping technique. For the first time in a triatomic molecule, a single charge state, in this case the trication, has been observed to dissociate into two distinct energy channels. With the aid of a three dimensional visualization technique to reveal the ionization hierarchy, evidence is presented for the existence of two sets of ionization pathways resulting from these two initial states. While one group of ions can be modeled using a Classical enhanced ionization model, the second group, consisting of mainly asymmetric channels, can not. The results provide clear evidence that an enhanced ionization approach must also be accompanied by an appreciation of the effects of excited ionic states and multi-electronic processes.

PACS numbers: 42.50.Hz, 33.80.Gj, 33.80.Wz

I. INTRODUCTION

Advances in tabletop femtosecond laser generation and amplification techniques has lead to the routine availability of light pulses which may be focussed to intensities comparable to the binding between the proton and electron in atomic hydrogen [1]. When a triatomic molecule is exposed to such a light pulse, the dynamics of electron removal and subsequent Coulomb explosion is rich in its complexity and not yet fully understood. Typically, the variation of the focussed laser intensity throughout the confocal volume [2, 3] exposes the molecule to $\simeq 10^{16}$ Wcm $^{-2}$ at focus, decreasing to such an extent that in the low intensity lobes before and after the focus that the effects are purely perturbative. Depending on the location and orientation of the molecule, the laser pulse can initiate a number of complex processes, including laser-induced reorientation [4], low energy dissociation with the removal of 0, 1 or 2 electrons [4, 5] and two- or three-body Coulomb explosion (2BCE and 3BCE respectively) [4, 6, 7, 8, 9, 10, 11, 12, 13, 14, 15, 16] with the removal of at least 3 electrons. Additional complexity is introduced through the observation that the laser pulse may modify the geometry of triatomics undergoing 3BCE (H₂O [6], OCS [7], CO₂ [4, 8, 9, 14, 15, 16], SO₂ [10], NO₂ [11]). The recent development of complete momentum measuring coincidence techniques, [17] and the advent of sub 10 femtosecond laser pulses has allowed the ob-

servation of the near equilibrium geometry of triatomic molecules through Coulomb imaging [18]. In addition both concerted and sequential dissociation channels have been mapped in time for SO₂²⁺[19]. Concerted and sequential channels in the triply charged ions of N₂O and CS₂ [20, 21, 22] have also been identified. 3BCE is further complicated in many-electron triatomics by the large number of possible ionization channels, here labelled according to the convention OCS^{(m+n+p)+} \rightarrow O^{m+} + Cⁿ⁺ + S^{p+} and referred to as the (m, n, p) channel.

Theoretical treatments of two- and three-body Coulomb explosion have been proposed and may be separated into quantum mechanical [23, 24] and classical [25] interpretations, broadly termed enhanced ionization (EI). However recent experimental and theoretical works present possible shortcomings. A number of theoretical considerations indicate that molecular ionization cannot be treated as the action of a single electron. Specifically, *ab initio* calculations of the distortion of carbon dioxide during multiple ionization by a static electric field [26] indicate the presence of a charge-exchange mechanism leading to experimentally observed geometries [4, 9] and ionization proceeding through the most negative atomic site. The ongoing theoretical investigation into the applicability of Thomas-Fermi theory to ultrafast ionization in molecules [27] has lead to a recent publication concerning the ionization of CO₂ and N₂O[28]. This hydrodynamic treatment of a group of active electrons has resulted in an impressive agreement between experiment and calculation, however the extent to which the predicted dynamics are physical is open to doubt. This is particularly clear in the case of Cl₂ [27] where the model generates

*Electronic address: w.bryan@ucl.ac.uk

a CI-CI bond much stiffer than is natural which subsequently plays an important part in keeping the molecule at low bond length as ionization proceeds.

An important consideration in molecular ionization is the sequence of events within the laser pulse temporal envelope. A strong coupling exists between electron removal and the expansion of the molecular bonds. Thus, as the molecule is ionized - either sequentially or non-sequentially, the rate of expansion of the molecular bonds can vary, strongly influencing further ionization. As proposed in enhanced ionization [25], a classical treatment of molecular ionization by Posthumus and coworkers, multiple ionization is governed by dissociation, which gives rise to sequential ionization every time a classical ionization threshold is crossed. The 'critical separation' in the bond length, where the final ionization takes place, is simply the consequence of the strong dip in the threshold intensity dependence on bond length. Typically, these critical separations are two or three times the ground-state equilibrium bond length depending on the molecular type. The threshold dip is the consequence of the combined effect of electron localization and Stark shifting. We have previously shown that the adaptation of this method to triatomics such as OCS can give quantitative agreement with experiment. A criticism of both the classical enhanced ionization treatment and hydrodynamic models is that neither makes any account the nonadiabatic response of a group of electrons to a laser pulse of a specific frequency and intensity, which has been shown to be influential [29]. Exact numerical solutions of the hydrogen molecular ion by Bandrauk and co-workers [23] have independently predicted a maximum in the ionization rate through a different mechanism. The electric field generated by the laser pulse produces a Stark-shift of the lowest-unoccupied molecular orbital (LUMO). For particular internuclear separations, this Stark-shifting lifts the LUMO above the Coulomb barrier. However, for ionization to proceed, the LUMO must be populated: as the molecule expands during the laser pulse, the exchange of population between the highest occupied molecular orbital (HOMO) and the LUMO becomes nonadiabatic, producing a net population in the LUMO. Furthermore, Kawata, Kono and Bandrauk have predicted similar maxima in the ionization rate in the case of linear H_3^+ in an intense laser field [30]. As in the case of H_2^+ [23], the response of the molecule to the laser field can be classified as either adiabatic or nonadiabatic. In the adiabatic system, electron transfer along the molecule is possible, whereas in the nonadiabatic case electron migration is suppressed due to laser induced localization. The ionization dynamics of this two-electron system depend heavily on both the electron distribution along the molecule and the nonadiabatic transitions between the lowest three electronic states.

These processes although not explicitly predicted for multi-electron systems have been the subject of some detailed experimental work [31, 32]. By making a careful examination of the bond lengths at which channels of

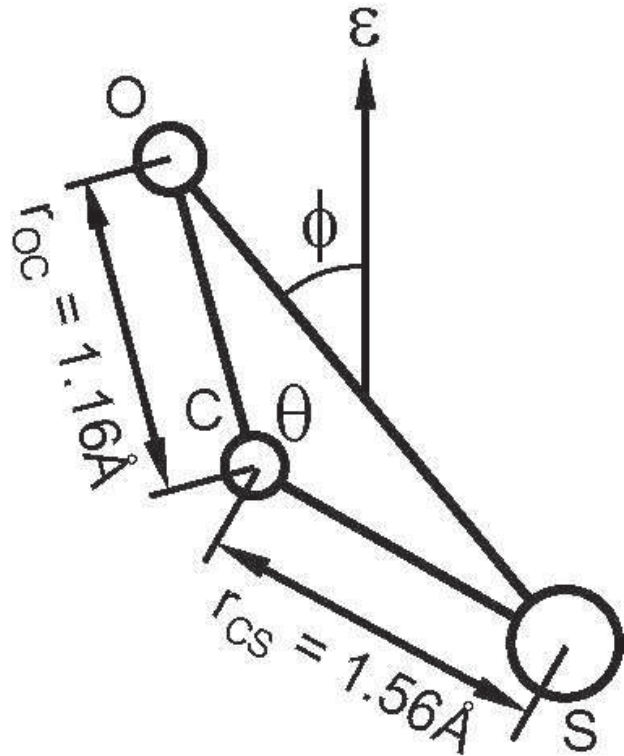


FIG. 1: Schematic of the carbonyl sulfide molecule currently under investigation.

the exploding N_2 and I_2 molecules appear to occur, it was deduced that certain channels could not be precursors of others and that because of this it was not possible that the symmetric enhanced ionization channel (1,2)-(2,2) could exist. It was therefore necessary to invoke multi-electronic processes causing asymmetric ionization pathways ie (1,2)-(1,3). The authors postulate that this process still involves the strong coupling of $g - u$ symmetry states (analogous to HOMO, LUMO in the enhanced ionization symmetric ionization process) but that the strong coupling of the outer electron to the field gives rise to the ionization of an inner electron (internal rescattering). Such multi-electronic processes would leave the molecular ion in excited states and direct evidence of this has been found in fluorescence studies of N_2 [33, 34] and various other molecules [35]. One innovative features of [32] was to introduce a visualize method able to show the progression of ionization through many available pathways.

In the case of a near-linear [7] triatomic such as OCS, the molecular geometry is defined by the bond lengths (r_{OC} and r_{CS}) and the bend angle (θ) between the bonds, as defined in figure 1, these are the controlling factors in EI. The current work continues our investigation of the behaviour of triatomics in a laser field; in the current work, we return to the carbonyl sulfide (OCS) molecule to resolve the ionization sequence. Our pre-

vious work [7] used momentum mapping and classical enhanced ionization to resolve the bond lengths at ionization for the 334 channel. We were able to show that the difference between the bond length calculated using a simplistic Coulomb assumption (the molecule is stationary before explosion) is within ten percent of the correct bond length calculated using an iterative technique. Although ionization channels have been identified in CO₂ [4, 12, 13, 15], and the possibility of non-sequential ionization taking place in order to reach the (111) channel has been discussed [36] the transitions between the higher channels have not been probed. By choosing the highly asymmetric OCS molecule instead of CO₂ we might expect to be able to find the limits of applicability of the classical ionization approach. Where possible our aim is to clarify the role of transitions between channels through the visualization of a hierarchical ionization topology.

The covariance mapping (CM) technique was used to investigate laser-molecule interactions as early as 1989 [37], but it was 1994 before exhaustive investigations into ionization in CO₂ were published. Frasinski *et al* [12] employed the technique to identify ionization channels; the observed channels were confirmed by Cornaggia *et al* [13] using a variant of the technique. Cornaggia performed further experiments on polyatomic molecules using CM, reporting a straightening of carbon dioxide in 130 fs laser pulses [14]. Without implying any compromise in the conclusions published by Cornaggia and co-workers, it has since become apparent that the CM technique is not ideally suited to investigating the geometry of exploding triatomics, which requires unit collection efficiency for all ions, irrespective of momentum. This situation was addressed initially by Hishikawa and co-workers who proposed the mass-resolved momentum imaging (MRMI) technique [9, 10, 11]. An analogue to this technique, ion-momentum imaging (IMI), was developed by the authors and co-workers, and applied to the 3BCE of H₂O [6], CO₂ [4] and OCS [7] where laser-induced geometry modifications were reported and compared to Monte Carlo simulations. Importantly, the IMI technique also includes an instrumental correction process [4, 6], that removes the instrumental bias by quantifying the variation of detector efficiency with ion species and momentum. W T Hill and co-workers examined molecular distortion by isolating 3BCE products from a specific channel and bend angle, then making comparisons between the EI and the Thomas-Fermi models [16]. This novel approach indicates the Thomas-Fermi and EI schemes may be linked via an effective charge defect.

In this paper, dissociation and 2BCE are investigated using two-dimensional covariance mapping (2DCM). Measurements of the kinetic energy of the product ions is reported. The 2DCM technique has previously been used to investigate 3BCE of CO₂ [4] and OCS [7], however, given that OCS is comprised of three different atomic species, and that the charge-to-mass ratio of oxygen and sulphur atoms is degenerate under certain ionization states, three-dimensional covariance mapping (3DCM) of

the Coulomb explosion of OCS is necessarily employed in the presented work. This allows unambiguous identification of the ionisation channels and measurement of their relative strengths. The kinetic energy release associated with each of these channels is also reported, allowing the OC and CS bonds to be measured. This paper is organised as follows: the experimental configuration will be discussed in the following section, with details of the data collection and processing. Results of 2DCM experiments will then be presented, and details of the observed OCS 2BCE channels introduced. The 3DCM of OCS will then be presented, with particular discussion concerning the application of modern visualisation techniques, allowing new insights into the behaviour of a triatomic during Coulomb explosion. Measurements of the r_{OC} and r_{CS} bond lengths will then be presented for each channel, along with an estimate of the relative channel strengths. At this point, the scheme of hierarchical ionization topology will be introduced, and the 3DCM results reinterpreted using a 3D diagrammatic technique adapted from [32].

II. EXPERIMENTAL CONFIGURATION AND DATA PROCESSING

As in previous experimental studies, the RAL (UK) ASTRA laser facility generated the femtosecond laser pulses, as detailed in previous publications [4, 6, 7, 8]. Ti: Sapphire seed pulses at 790 nm were amplified by CPA [38] to a pulse energy of 1 mJ in 50 fs at a repetition rate of 10 Hz. An $f/5$ focus was then generated in the source region of a Wiley-McLaren [39] time-of-flight mass spectrometer (TOFMS), interacting the laser pulses with the gas target. The background pressure in the TOFMS system is $\simeq 8 \times 10^{-10}$ mbar. Product ions generated by the interaction of the focused laser pulse with the target gas were extracted from the source region, and detected using a pair of micro-channel plates after 11 cm of field-free drift. Throughout the present work, the laser polarization direction is parallel to the axis of the TOFMS. Unlike previous IMI experiments, the detector is now exposed to the full confocal volume and operated in high efficiency mode, with an extraction field of 600 Vcm⁻¹. The output of the TOFMS is monitored on a Tektronix TDS-744A digital storage oscilloscope (DSO). Time-of-flight spectra were recorded on the DSO, and stored on a laboratory PC for off-line analysis. The two- and three-dimensional covariance coefficients ($C_2(x, y)$ and $C_3(x, y, z)$ respectively) were then evaluated for all n points for each of the N TOF spectra. For definitions of $C_2(x, y)$ and $C_3(x, y, z)$, the reader is referred to reference [40], which provide full discussions of the application of covariance mapping to molecular ionization. Depending on the process under investigation, either $C_2(x, y)$ (2BCE) or $C_3(x, y, z)$ (3BCE) was evaluated for all n points on the TOF spectrum, resulting in an n^2 matrix in the case of $C_2(x, y)$, referred to as the two-dimensional covariance

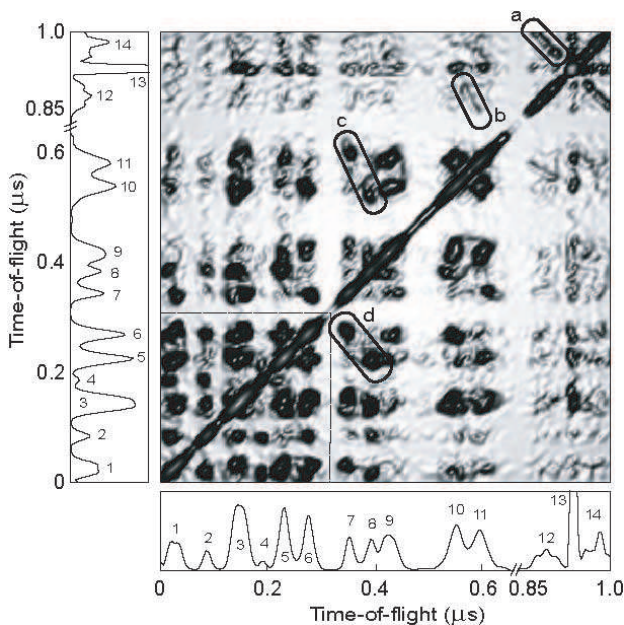


FIG. 2: Two-dimensional covariance map of carbonyl sulfide recorded with 790 nm 50 fs Ti: Sapphire laser pulses focused to an intensity of $\simeq 10^{16}$ Wcm $^{-2}$. The regions of positive covariance are identified by the labelled average time-of-flight spectra, the peaks are identified in table 1. The features identified *a - d* are discussed in the text.

map (2DCM) and an n^3 matrix in the case of $C_3(x, y, z)$, similarly referred to as the three-dimensional covariance map (3DCM). Throughout this paper, the axes x, y are defined as the time-of-flight axes in the 2DCM, and x, y and z are defined as the time-of-flight axes in the 3DCM.

To test the performance of the experimental apparatus with respect to false correlations [40], a series of two-dimensional maps were recorded for the order of 3000 laser shots as a function of target gas pressure. At a target gas pressure of 3×10^{-9} mbar, the contribution of false correlations to the covariance map became negligible. Of the order of 10^5 individual TOF spectra were recorded directly to hard disk.

III. RESULTS - 2BCE OF OCS

Figure 2 is a surface representation of the 2DCM of OCS after 10^4 laser shots, under the optical conditions discussed in the previous section. Correlations on the map are identified by labeled average time-of-flight spectra to the left and below the map, where the peaks in the ionization signal are identified in table I. As is apparent from table I, peaks 3, 5, 6, 10 and 11 are the result of the detection of two or more ions, either through charge degeneracy (peaks 5, 6, 10 and 11) or temporal overlap. As a consequence, the average time-of-flight spectrum gives a limited amount of information about the explosion of the molecule. Note that both TOF axes are truncated

TABLE I: Peak assignments for the average time-of-flight spectra presented in the present work

| Peak | Ion Species |
|------|--------------------------------|
| 1 | C^{3+} |
| 2 | O_F^{3+} |
| 3 | $C^{2+} / O_B^{3+} / S_F^{5+}$ |
| 4 | S_B^{5+} |
| 5 | O_F^{2+} / S_F^{4+} |
| 6 | O_B^{2+} / S_B^{4+} |
| 7 | S_F^{3+} |
| 8 | S_B^{3+} |
| 9 | C^+ |
| 10 | O_F^+ / S_F^{2+} |
| 11 | O_B^+ / S_B^{2+} |
| 12 | $CO_{F/M/B}^+$ |
| 13 | OCS^{2+} |
| 14 | $S_{F/B}^+$ |

between peaks 11 and 12, as no ions are detected between $t = 650$ and 850 ns. The major features of figure 2 are as follows. The strong diagonal signal is the autocorrelation line, a consequence of an event at $x = y$ always being self-correlated and therefore gives no information about the processes under investigation. True correlations lie above and below this line, false correlations associated with peak 13 (OCS^{2+}) are unavoidable. The double ionization of the molecular ion requires a lower intensity as compared to the multiple ionization leading to Coulomb explosion, hence the volume of the focus generating OCS^{2+} is approximately an order of magnitude greater than that generating the Coulomb explosion signal [2].

Important features of figure 2 are highlighted *a - d*, and are identified thus: (a) $CO^+ + S^+$, (b) $CO^+ + S^{2+}$, (c) $S^{3+} + O^+$ and (d) $S^{3+} + O^{2+}$. Correlations (a) and (b) identify the 2BCE channels (1, 1) and (1, 2) respectively. The kinetic energy release (KER) associated with these 2BCE processes, channels *a* and *b*, may be calculated from the temporal width in x and y of the correlations, and are presented in table II. These channels, (1,1) and (1,2) are expected in the 2DCM, as the OC bond is considerably stronger than the CS bond, as observed in recent dissociative photoionization experiments performed by Eland and co-workers [41] and Brion and co-workers [42], implying that early ionization and dissociation favour energetically efficient routes. Wang and Vidal [43] have published cross sections for the electron impact dissociative ionization of OCS, and reported the $CO^+ + S^+$ channel has a cross section at least five times that of any channel involving CS^+ . In the present work, only a trace of CS^+ is detected at a longer flight time than that presented in figure 2, however it is uncorrelated on an equivalent 2DCM, implying $O^+ + CS^+$ is negligible, and the CS^+ signal probably originates from the very weak $O + CS^+$ dissociative process.

Because of the charge degeneracy and temporal overlap

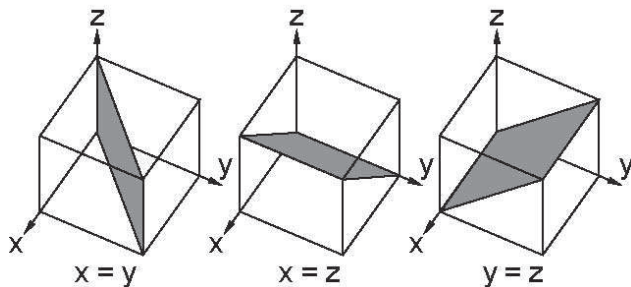


FIG. 3: Geometry of the autocorrelation planes present in a three-dimensional covariance map

present in much of the average time-of-flight spectrum, the dense area of the 2DCM containing the atomic product ions where $t \leq 0.65 \mu s$ is difficult to interpret. However, relying on the fact that peaks 7 and 8 are purely due to S^{3+} , correlations (c) and (d) can be employed to make limited inferences about the molecular behaviour. Correlations (c), peaks 7 (S_F^{3+}) and 11 (O_B^+ / S_B^{2+}) peaks 8 (S_B^{3+}) and 10 (O_F^+ / S_F^{2+}) are forwards - backwards pairs, formed by the ions being produced parallel to the laser polarization direction. Similarly in correlation (d) peaks 7 (S_F^{3+}) and 6 (O_B^{2+} / S_B^{4+}) and peak 8 (S_B^{3+}) and 5 (O_F^{2+} / S_F^{4+}) are forward backward pairs. As observed in [7] the molecule favours exploding with the O - S axis aligned to the laser field, i.e. $\varphi = 0$ in figure 1. All triatomic molecules exposed to similar laser conditions have been found to exhibit this forward-backward behaviour. However other correlations are overlapping such as those associated with peak 3 which represents C^{2+} as well as O_b^{3+} and S_f^{5+} .

IV. RESULTS - 3BCE OF OCS

To establish the 3BCE channels, we turn to the 3DCM results. Due to the extra dimension introduced into the calculations, the correlation islands on the 2DCM, figure 2, become correlation volumes in the 3DCM. True 3BCE correlations appear as small volumes of positive covariance within the map volume. Identifying the locations of these correlations is complicated by the presence of three autocorrelation (AC) planes, which traverse the map at $x = y$, $x = z$ and $y = z$. As with the AC line in a 2DCM, volumes of the 3DCM located on the AC planes have a stronger covariance than 3BCE correlations but are essentially meaningless. The geometry of the AC planes is illustrated in figure 3, and will be present in any 3DCM.

Research Systems IDL (Interactive Data Language) 5.5 was used to examine the OCS 3DCM, allowing us to present, for the first time, visualizations through the body of the 3DCM. Previous studies [12, 13, 15, 40] present two-dimensional slices through the body of the 3DCM, where a slice or plane parallel to the x -axis shows all correlations in y and z . While being a reasonable man-

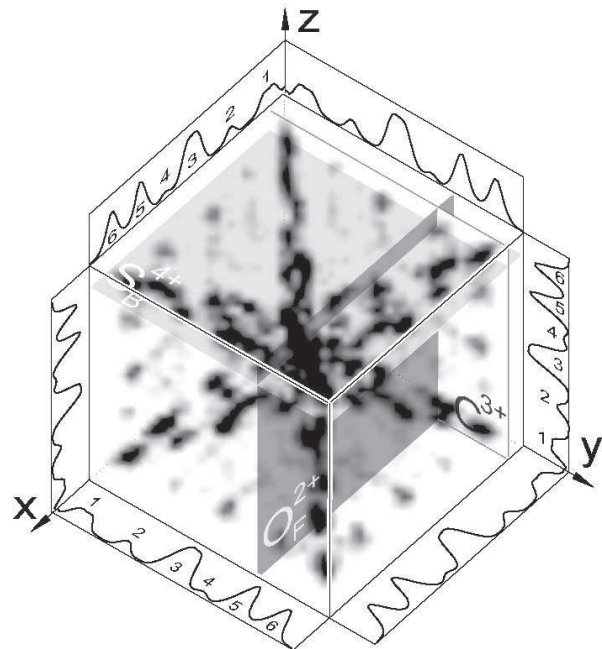


FIG. 4: Projection visualization of the OCS three-dimensional covariance map. The range in (x, y, z) corresponds to the region within the dashed box in figure 2. The peaks are identified by comparison with table I. Three semitransparent planes illustrate the location of the (2, 3, 4) channel.

ner in which to view a complex dataset, when viewed in three-dimensions, the location of local maxima may be identified more easily and accurately. A voxel (volume element) projection of the 3DCM between $0 \leq (x, y, z) \leq 300$ ns is presented in figure 4, corresponding to the region in figure 2 between the origin and the dashed lines. The full 3DCM was calculated up to $t = 1$ ms, but for the purposes of presentation, only a limited subset of this volume presented in figure 4.

The visualization presented in figure 4 is generated in two steps. Firstly a transparency threshold, T is defined such that if $C_3(x, y, z) \leq T$, the point (x, y, z) is treated as transparent. If $C_3(x, y, z) > T$, the point (x, y, z) is assigned a variable opacity, where the opacity depends logarithmically on $C_3(x, y, z)$. Secondly a three-dimensional transform is applied allowing arbitrary rotation, translation and oblique display of the 3DCM onto an image plane, in this case defined as the plane of the figure. Visualization in this manner is similar to taking an x-ray of the dataset, with the covariance coefficient equivalent to density, thus dark regions of figure 3 correspond to volumes of high covariance. The position of the AC planes in figure 4 may be identified through a comparison with figure 3. The dark volumes between the AC planes are true correlations, generated only by 3BCE channels, identified in part by average TOF spectra displayed parallel to the x, y, z axes. The labels on

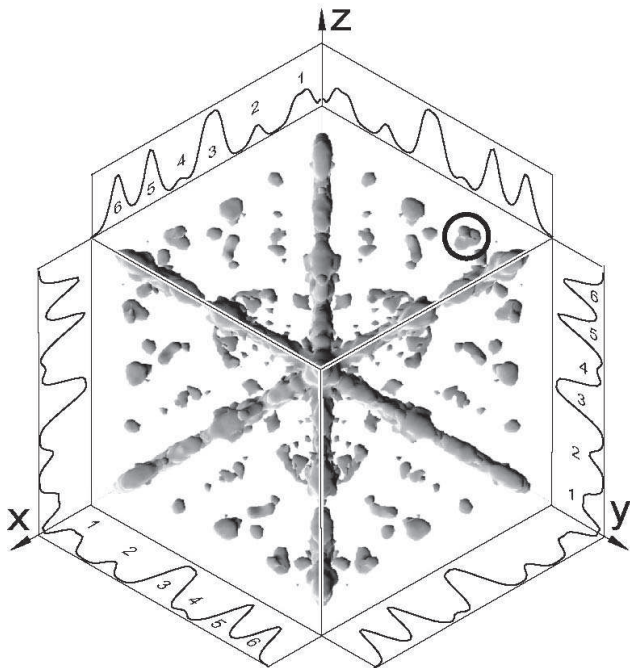


FIG. 5: Iso-surface visualization of the OCS three-dimensional covariance map, where the complication of the dataset by the presence of the three autocorrelation planes has been almost negated by viewing the map along the direction $x = y = z$. Again, the peaks are identified by comparison with table I. The circled region corresponds to the three-body correlation forming the (2, 3, 4) channel.

the average TOF spectra adhere to the peak assignments in table I.

An example of a 3BCE correlation between peaks 1 (C^{3+}), 5 (O_F^{2+} / S_F^{4+}) and 6 (O_B^{2+} / S_B^{4+}) is identified in figure 4 by the intersection of three semi-transparent planes superimposed in the 3DCM. This correlation therefore represents the (2, 3, 4) channel, where the ion order has been changed to agree with the (m, n, p) convention discussed earlier. However, the KER associated with this channel cannot be measured, as there is uncertainty due to the charge-to-mass degeneracy as to whether axes y and z represent O_F^{2+} and S_F^{4+} respectively or vice versa: the solution of this problem will be presented later in this section.

Figure 5 is an iso-surface representation of the 3DCM, an iso-surface being the 3D equivalent of a contour in 2D. The image plane in figure 5 is defined normal to the line $x = y = z$, dramatically reducing the impact of the AC planes, as each of the AC planes $x = y$, $x = z$ and $y = z$ are normal to the image plane. A series of iso-surfaces is used to examine the 3DCM, thus identifying the 3BCE channels, where true correlations are identified in the regions between the AC planes by adjusting the iso-surface threshold. The $C_3(x, y, z)$ volume is investigated by varying the surface threshold and noting local maxima in the regions bounded by the AC planes,

TABLE II: Kinetic energy release (KER) associated with all 2BCE and 3BCE channels as identified from the 2DCM and 3DCM. The r_{OC} and r_{CS} bond lengths are modeled using a Monte Carlo method, and the channel strength is estimated by integrating the covariance volumes.

| Channel | KER (eV) | r_{OC} (Å) | r_{CS} (Å) | Strength (arb.) |
|----------|----------|--------------|--------------|-----------------|
| (1,1) | 4.1 | - | 2.9 | 0.5 |
| (1,2) | 7.6 | - | 3.2 | 0.2 |
| (1,1,1)a | 12.3 | 2.5 | 3.5 | 0.7 |
| (1,1,1)b | 14.9 | 2.0 | 3.0 | 1.0 |
| (1,1,2) | 17.9 | 2.6 | 3.7 | 1.5 |
| (1,2,2) | 34 | 2.3 | 3.5 | 2.0 |
| (1,2,3) | 38.9 | 2.8 | 3.9 | 1.0 |
| (2,2,2) | 46.3 | 2.6 | 3.8 | 1.5 |
| (1,2,4) | 48.3 | 2.5 | 4.1 | 1.0 |
| (2,2,3) | 55.8 | 2.7 | 4.0 | 3.0 |
| (2,3,2) | 59.6 | 2.8 | 4.2 | 2.5 |
| (1,3,4) | 66 | 2.6 | 4.2 | 1.0 |
| (2,2,4) | 63 | 2.9 | 4.3 | 4.0 |
| (2,3,3) | 73 | 3.0 | 4.1 | 4.0 |
| (2,3,4) | 81 | 3.1 | 4.5 | 5.0 |
| (3,2,4) | 78 | 3.2 | 4.4 | 2.0 |
| (3,3,4) | 96 | 3.3 | 4.9 | 4.0 |
| (3,3,5) | 105 | 3.4 | 5.2 | 2.0 |

corresponding to 3BCE channels. The primary benefit of 3D visualization is that by moving the viewpoint from parallel to the x , y or z axes, an analogue to taking a slice, to a point on the line $x = y = z$ simplifies the system considerably. Furthermore, by examining volumes of the map rather than slices, a more accurate identification may be carried out, effectively removing the AC planes from the dataset and thus making the volumes of interest immediately accessible.

The KER associated with each of the correlations identified is calculated from the time difference between the centre of the correlation volume and the zero kinetic energy point for each ion charge-to-mass ratio parallel to the x , y , z axes. The total KER associated with each correlation volume is presented in table II, along with an estimate of the relative strength of the channel in the range 0 to 5. The detected channel strength is gauged by integrating the correlation volumes. Returning to identifying the correlations highlighted in figures 4 and 5, by converting the KER (eV) to momentum, p (amu ms^{-1}) for all combinations of ion identities possible from table I, a straightforward application of the conservation-of-momentum parallel to the detector axis allows the correct bond length assignment to be made. An incorrect assignment of the 3DCM correlation volume results in a net momentum imbalance, whereas a correct assignment leads to zero net momentum. This process is repeated for each correlation volume in figures 4 and 5, and for all possible ion assignments for a particular group of three peaks, thus the 3BCE channels are unambiguously identified. The final assignments are presented in table II.

In the case of a diatomic molecule Coulomb exploding,

it is trivial to estimate the bond length at the point of explosion [25]. However, in the case of 3BCE of OCS, which, as apparent from table II, is heavily predisposed to charge-asymmetric Coulomb explosion, such a calculation is not straightforward. To address this, the following technique was applied. The bend angle (θ) distribution between r_{OC} and r_{CS} (see figure 1) for identical laser conditions is known [7], and using the Monte-Carlo software developed as part of our IMI technique [4, 6, 7], the 3BCE of OCS is simulated in momentum space for a range of geometries. The bond lengths reported in table II are those in strongest agreement with the 3DCM presented in figures 4 and 5, with r_{OC} , r_{CS} and θ bound by conservation of momentum. As discussed earlier these bond lengths assume a coulomb explosion from a stationary molecule. Although this is clearly not the case, previous work [7] suggests that even for the highest channels the discrepancy is around 10% between this approximation and the correct bond length, and so rather than embark on the iterative process set out previously [7] we will begin our analysis with these approximate values. A number of general trends are observed in table II: there is an overall increase in the KER with increasing channel order, an observation common to Coulomb explosion studies [4, 7, 9, 11, 12, 13, 15], caused by the higher Coulomb repulsion between the ionic constituents. Furthermore, the r_{OC} and r_{CS} bonds are generally asymmetric throughout, and tend to increase with channel ionization, $q = (m + n + p)$. Importantly, two (1, 1, 1) channels are observed in the 3DCM, labeled (a) and (b) in table II in order of increasing KER. There should clearly be a dynamic coupling between the 3BCE channels presented in table II, however the tabulation of the results is somewhat ambiguous.

V. DISCUSSION

To comprehend the possible pathways which the OCS molecule can take during ionization we first make the assumption that the ionization channels which we observe are the steps on an ionization ladder which finishes at (335). To visualize this we have adapted the method of [32] into a 3D hierarchical ionization topology. The general hierarchical ionization (GHI) diagram for laser-OCS interaction is presented in figure 6, where the ionization channels presented in table II, identified from the 3DCM presented in figures 4 and 5 are indicated as nodes on a pyramidal framework. The least-charged (lowest order) channel (1, 1, 1) is the node at the apex of the pyramid, corresponding to a total charge, $q = 3$. Progression down the pyramid from the apex between the subsequent triangular grids indicates ionization through the loss of one or more electrons. Each intersection on a particular triangular grid uniquely represents a channel. Three classes of node are introduced in figure 6: (1) each intersection represents a numerically possible channel, (2) the open circles represent an experimentally possible channel, and

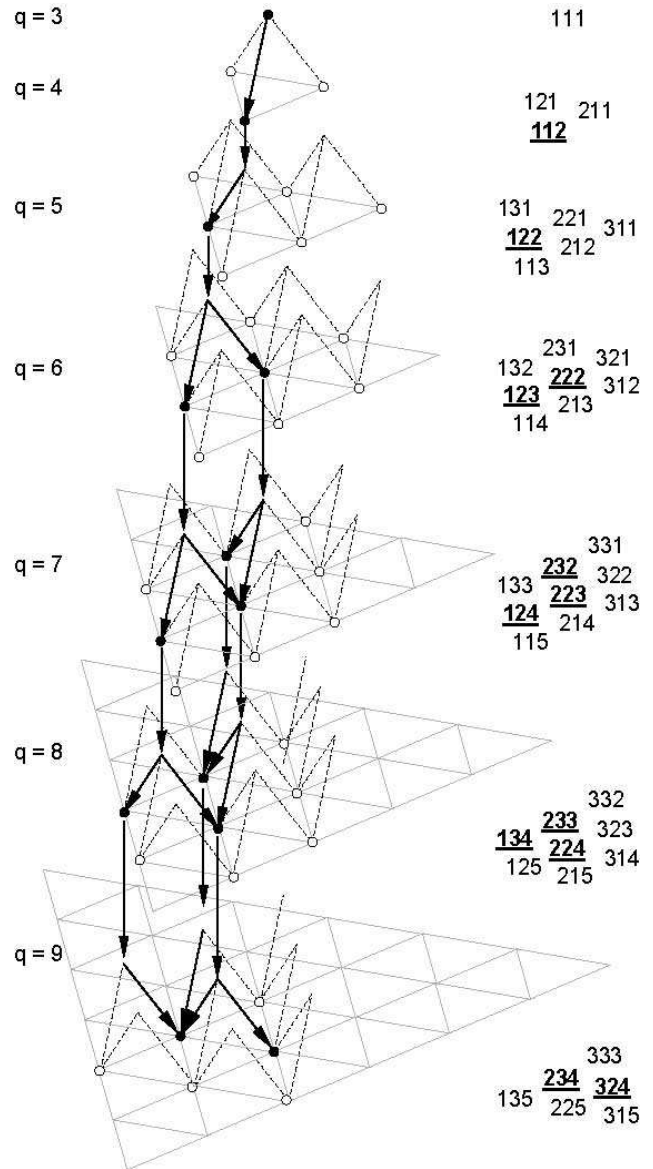


FIG. 6: General hierarchical ionization (GHI) diagram for the 3BCE channels observed in the 3DCM as presented in table II. Open circles represent numerically possible channels, solid circles represent true 3BCE channels.

(3) the filled circles represent observed 3BCE channels. The refinement to these three classes of node makes the distinction between whether an ion may be generated, is observed in the average time-of-flight spectrum or is observed as a true 3BCE channel, following the application of conservation of momentum as discussed earlier. The key to the right of figure 6 indicates experimentally possible channels (regular type) and observed 3BCE channels (bold underlined). For example, on the $q = 9$ level, 28 channels are numerically possible, illustrated by the large basic grid. However, the necessary component ions are only observed for six channels (indicated in the key), and of these six, only two triply-correlated channels are ob-

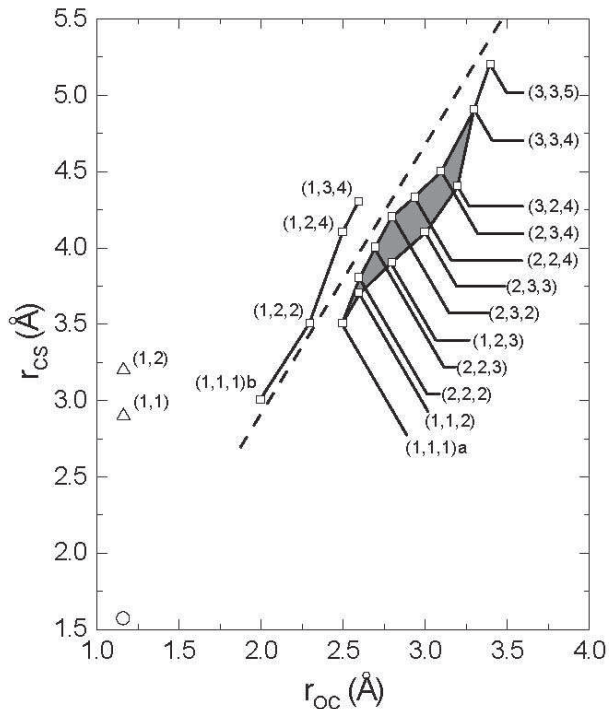


FIG. 7: The 3BCE channels identified from the 3DCM presented in (r_{OC}, r_{CS}) space, forming the second stage in hierarchical ionization topology. The two groups of 3BCE channels observed are separated by a dashed line for clarity.

served in the 3DCM for this level. The vertical arrows in figure 6 indicate the transfer between q -levels, the heads of which reach the vertices of three-sided secondary pyramids on the next q -level. At this point the overall charge of the molecule is known, but the specific ionization channel is not. The ionization routes emanate from the vertex of the secondary pyramid. In choosing one of the three sides of this pyramid, the ionization channel is specified. At this point, molecular ionization is treated as a single-site sequential process. GHI is well illustrated by the transition between the $(2, 2, 3)$ channel on the $q = 7$ level and the $(2, 2, 4)$ and $(2, 3, 3)$ channels on the $q = 8$ level.

The most striking feature of figure 6 is the apparent profusion of ionization routes through the GHI diagram. We now turn to the second stage of hierarchical ionization topology, and consider the influence of the geometry of the exploding molecule as it develops through the GHI diagram. Figure 7 shows the result of plotting in (r_{OC}, r_{CS}) space all of the ionization channels uniquely identified using 3DCM. The first observation which is clear from figure 7 is that the approximate bond lengths are not particularly constant as would be expected from an enhanced ionization explanation, although on further inspection they do form a group centered around extended bond lengths of $r_{CS}=3.7\text{au}$ and $r_{OC}=2.7\text{au}$ which would correspond 2.5 and 2.25 times the equilibrium bond lengths which is similar to the factor of 2, observed for CO_2 [4].

The second observation is that both bond lengths increase with charge state but in an oscillating fashion (see shaded area figure) [7]. This increasing trend is similar to that observed previously for CO_2 [9]. In addition the oscillation is accompanied by a set of channels somewhat offset from the others. Specifically, the group of 12 3BCE channels, starting with $(1, 1, 1)\text{a}$ and finishing at $(3, 3, 5)$ contains the majority of channels, which are generated at larger r_{OC} and r_{CS} locations. The channels $(1, 1, 1)\text{b}$ to $(1, 3, 4)$, are generated at smaller r_{OC} and r_{CS} as compared to the main group. The dashed diagonal line running from bottom left to top right serves as a visual guide, separating the two regions of (r_{OC}, r_{CS}) . For illustrative purposes three solid lines link the ionization channels. At this point we must be very careful about the conclusions we draw. It is tempting to see the bond information, in table II and in figure 7, as being indicative of those bond lengths occupied during the steps in the ionization ladder illustrated in figure 6, and this is exactly the procedure carried out by [27, 31, 32], although the bond lengths are calculation differently to here in [31, 32]. But it is important to realize that however accurate the bond length measurement are, for a particular ionization channel say (223) , it does not mean that this ionization state uniquely occurs at the measured bond lengths. A higher ionization state, say (233) , formed in a region of the focus of higher peak laser intensity, might display the same bond lengths because of enhanced ionization. In this case the molecule could still have passed through the (223) state, but at shorter bond lengths. This is best illustrated for OCS by figure 8 in [7] which shows that although each channel may ionize last at the critical distance the precursors to any given channel will ionize at shorter bond lengths. These shorter bond lengths are not measurable with a long laser pulse. This phenomenon is consistent with the recent work using short (sub 7fs) laser pulses [18, 19] which clearly shows ionization at bond lengths less than the critical distance, if ionization is switched off rapidly before the critical distance is reached. For pulses of 50fs or longer, it is even possible that bond lengths measured for say the (233) channel could be shorter than those measured for the (223) channel but that the (223) state is a precursor of the (233) channel. Two 2BCE channels are also included in figure 7. It is assumed that the OC bond has not expanded during 2BCE, thus 2BCE can be thought of as starting from the equilibrium geometry (\circ , figure 7), then the CS bond expands while the OC bond is constant, undergoing ionization to the $(1, 1)$ or $(1, 2)$ channels (Δ , figure 7). Furthermore the dissociation of OCS into both $(1, 1)$ and $(1, 2)$ will be quite nonCoulombic and so the approximate bond lengths given in figure 7 are expected to be an overestimate. It is even likely that these channels dissociate from equilibrium.

Figure 7 makes a distinction between two regions in (r_{OC}, r_{CS}) space. In the case of the four channels to the left of the dashed diagonal line, multiple ionization only occurs from the carbon or sulphur sites. The charge on the oxygen site remains 1, even though the carbon is

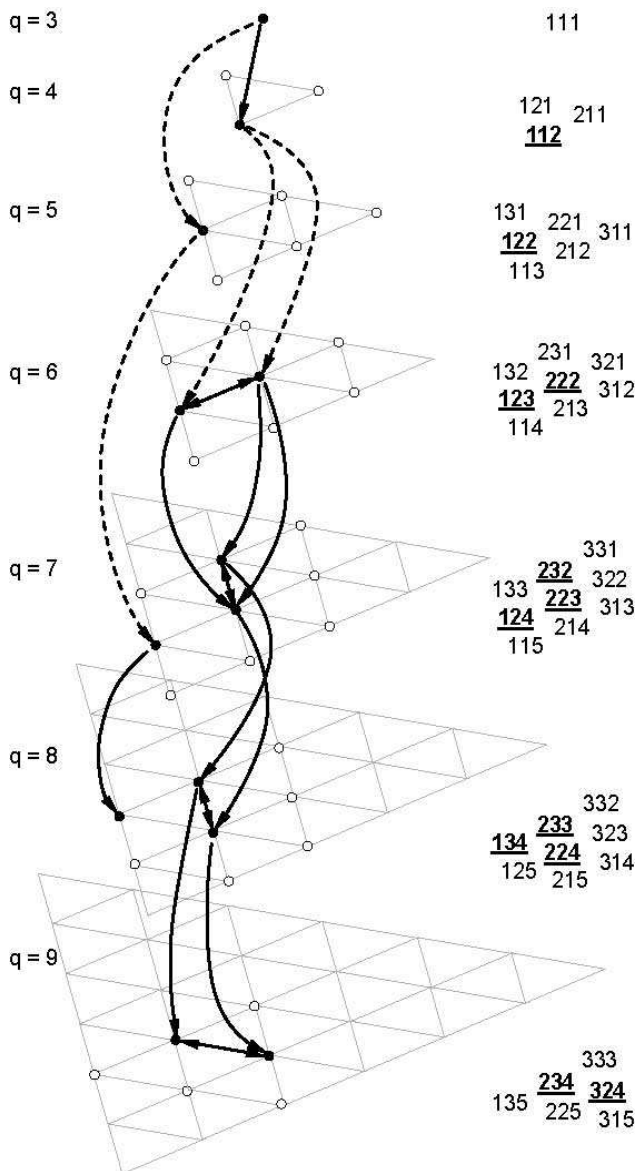


FIG. 8: Refined hierarchical ionization (RHI) diagram for the 3BCE channels observed in the 3DCM after simplification as described in the text. The solid arrows indicate single ionization, the dashed arrows indicate double ionization.

observed to loose up to 2 more electrons and the sulphur up to 3 more. In contrast, the channels to the right of the dashed line in figure 7 are observed to Coulomb explode with levels of ionization loosely bound by the ionization potentials of the constituent atoms. At this point we tentatively proposed that the (111)*b* channel and the asymmetric channels are associated and form a different ionization ladder to the channels to the right of the line.

Figure 8 illustrates the refined hierarchical ionization (RHI) diagram for the laser-OCS interaction. Visually, figure 8 appears simpler and better defined in comparison to figure 6 as there are fewer connections between nodes;

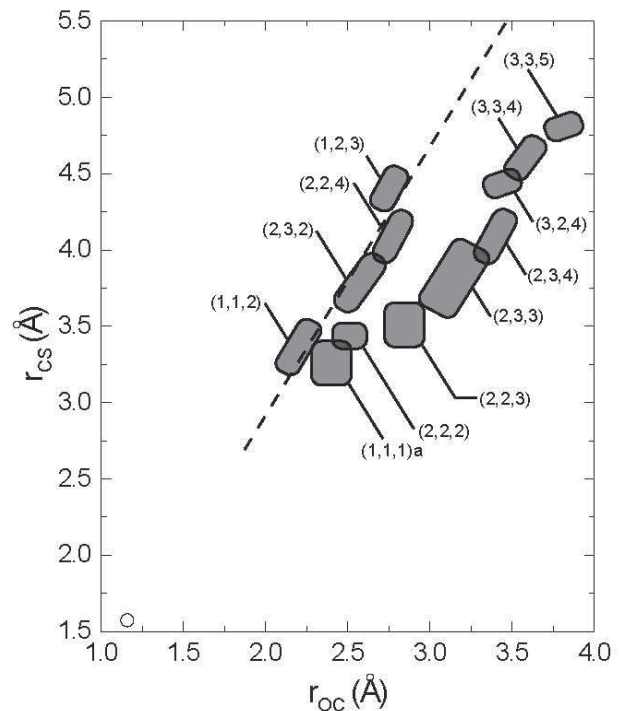


FIG. 9: Simulation of ionization to the right of dashed line in figure 7, using the modified enhanced ionization (EI) model, described in the text. An analogous simulation of channels to the left of the line was unsuccessful.

however, the processes implied are significant. The three 3BCE asymmetric channels which are observed after the (111)*b* channel are generated through two stages of double ionization. Dashed lines in figure 8 indicate a double ionization step. A pair of double ionization steps also occur after the (111)*a* channel on route to (1,2,3) and (2,2,2) from (1,1,2).

We now attempt to reproduce the results to the right of the dashed line in figure 7 using the results of a series of EI calculations. Unlike the previous calculations presented in [7], the current calculations allow both bonds to expand independently, thus for each (m, n, p) channel an appearance intensity surface is created in (r_{OC}, r_{CS}) space. This large calculation is possible by only calculating the effective Coulomb potential (Coulombic and laser field) along r_{OC} and r_{CS} , as it has been found that this potential is minimized along these axes, hence EI will depend only on these conditions. This simplification only applies for near linear molecules (in this case $\theta = 170$ degrees) parallel to the laser polarization direction, reasonable in this case given the observations of Sanderson *et al* [7]. To best replicate the laser conditions responsible for the observations of figure 7, a wide range of laser intensities are modeled, as the laser intensity defines which ionization channel occurs. Each channel occupies a region of (r_{OC}, r_{CS}) space, indicated by the shaded areas in figure 9. As is apparent from comparison between figures 7 and 9, there is reasonable agreement between the

measured and predicted distribution in (r_{OC}, r_{CS}) , especially given the number of ionization channels involved.

As a development of the original treatment of the Coulomb explosion of diatomic molecules [25], the reasonable agreement between the figures 7 and 9 is only possible following two major modifications to the model. Firstly, using the accepted ionization potentials of the constituent atoms, the appearance intensity minimum in (r_{OC}, r_{CS}) space (the critical geometry) is considerably larger than equilibrium for low q channels, and moves to lower r_{OC}, r_{CS} with increasing total charge q . So, even before taking into account the laser pulse trajectory [25], the trend observed in figure 7 cannot be replicated within the unmodified EI model. By decreasing the atomic ionization potentials with increasing charge, the appearance intensity minimum is varied to give a far better agreement with the present observations. The best-fit ionization potential $I_p' = k I_p$ where I_p is the accepted ionization potential and k is the scaling parameter given by $k = -0.1(m, n) + 1$ or $k = -0.05p + 0.95$ depending on the channel (m, n, p) . Secondly, calculating the laser trajectory as the molecule expands reveals a dramatic underestimate of the bond extension for all channels, for example, the unmodified model predicts the (3,3,5) channel Coulomb explodes from $r_{OC} = 2.5 \text{ \AA}$, $r_{CS} = 3.0 \text{ \AA}$. Careful investigation of the intersections between the appearance surfaces and the laser trajectories over a wide intensity reveals the low q channels ionizing with near equilibrium bonds, thus limiting the expansion possible in the higher q channels. The behaviour of the low q channels indicates that molecular expansion is not purely Coulombic, a simple solution to the overestimate of the interaction is to reduce the charge of the ions by assigning fractional charges, adjusted to give a best fit to figure 7. It was found that the low q channels, i.e. (111), required charge suppression ≈ 0.7 , whereas the high q channels, i.e. (335) needed no charge suppression, intermediate channels exhibit a linear relationship between these limits.

The modifications made to the enhanced ionization model do have valid physical basis. Firstly the modifications to q effectively introduce a bonding aspect to the low charge states and make them less Coulombic. This deviation from pure Coulomb interaction for low charge states is well known in such molecules as Cl_2 [44] and decreases with charge state. The small modification to the atomic IP's can be related to the ionization potential of the molecule, or the gap between the molecular interaction potentials. For low charge states the gap is larger than it would be for purely Coulombic interactions because the bonding character of the potential, represented by a dip below the Coulombic curve, reduces in magnitude as charge state increases. With these modifications it is possible to represent the general features of the majority of the ionization channels, in a way which is self consistent throughout and this is a significant indication of the overall validity of the enhanced ionization model. However it is equally significant that we can not repre-

sent all final ionization channels with this approach. The (111)*b* channel and the other channels to the left of the dashed line in figure 7 can not be accommodated by this treatment.

In an effort to account for the remaining channels we should begin by explaining the two distinct energy groups for the (111) channel. Firstly it is sensible to consider enhanced ionization as it has been reasonably successful thus far. In the enhanced ionization picture bond expansion towards the critical distance is required before CE is complete. This would seem to imply the existence of two critical distances for the (111) channel. Although a secondary minimum was found in the ionization threshold curve calculated for the (334) channel previously [7] none was found for the (111) channel. Even if a double structure does exist for an ionization threshold curve it does not easily give rise to double valued bond lengths, because if an ionization trajectory crosses the threshold curve once, the molecule will ionize and there is no advantage to crossing more than once. A second possibility is the presence of two distinct energetic channels in the break up of OCS^{3+} , this might be more likely as we observe stable OCS^{3+} in the time of light spectrum of this molecule, a quite unusual observation for triatomic molecules; it is not seen for CO_2 or N_2O for instance. It is possible that a long lived metastable trication may completely dissociate after the laser pulse from equilibrium geometry. The (111)*b* channel appears to have stretched from equilibrium but this could be deceptive just as r_{CS} appears to have stretched in the (11) and (12) channel this may just be the effect of a non Coulombic dissociation channel. One problem with this possibility is that (111)*b* appears to be precursor of the other channels such as a s (122) and this could not take place after the laser pulse. A third possibility is that two distinctive dissociation channels in the OCS^{2+} molecule exist, which give rise to different degrees of atomic excitation. The more highly excited molecule would ionize to the (111) channel at a lower laser intensity, this phenomenon has been observed for metastable argon ions [45]. A consequence of this would be to shift the critical distance to lower bond length, in fact two curves would exist for the two different molecular states with the same charge. It should be noted that two distinct kinetic energy groups have been observed for the S fragment in the $\text{CO}+\text{S}$ dissociation of OCS after 233nm absorption [46]. This phenomenon could not be predicted from the simple classical mode, as it would require two distinct sets of atomic ionization potentials to exist. Excited molecules formed in high intensity regions would reach the (111) channel earlier in the laser pulse and this may be why asymmetric double ionization is possible after the (111)*b* channel is formed, as multi electronic asymmetric processes occur at bond lengths closer to equilibrium than the critical distance [32]. If asymmetric ionization is preferred at shorter bond lengths then only the state which gives rise to the (111)*b* channel can make the triply ionized molecule at sufficiently small bond length to allow further asymmetric

multi-electronic processes to occur. The state which give rise to the (111)*a* channel does not do so until after the molecule has passed through this bond length range.

VI. CONCLUSION

The kinetic energy release during two- and three-body Coulomb explosion of carbonyl sulfide has been measured using three-dimensional covariance mapping. For the first time in a triatomic molecule two distinct energy groups have been identified for the same dissociation channel. A 3D hierarchical ionization topology has been introduced to help visualize the multitude of possible ionization pathways and a Classical trajectory simulation using a simple over the barrier enhanced ionization model has been used in an attempt to reproduce the observed bond lengths. The distribution of most bond lengths are reasonably predicted when small modification to the enhanced ionization model are introduced. The presence of the two (111) channels and highly asymmetric channels

however can not be modeled using the simple approach.

In conclusion, OCS has proven to be a useful subject of study in the quest to understand the ionization mechanisms of small molecules in an intense laser pulse. The results indicate the need to develop an enhanced ionization model which incorporates molecular excitation and the possibility of multi-electronic processes in order to be able to fully predict the ionization process. In addition the need for further experimental study is indicated, in order to better understand the interplay between the ionization routes indicated by the current work, utilization of sub 10 femtosecond pulses would enable probing within the critical distance and full coincidence techniques would establish the link between geometry and ionization pathway.

Acknowledgments

This work is supported by the Engineering and Physical Sciences Research Council, and NSERC.

-
- [1] S. Backus, C. G. D. III, M. M. Murnane, and H. C. Kapteyn, *Rev. Sci. Instrum.* **69**, 1207 (1998).
- [2] A. El-Zein, P. McKenna, W. A. Bryan, I. M. G. Johnston, T. R. J. Goodworth, J. H. Sanderson, I. D. Williams, W. R. Newell, P. F. Taday, E. J. Divall, et al., *Physica Scripta* **T92**, 119 (2001).
- [3] M. A. Walker, P. Hansch, and L. D. V. Woerkom, *Phys. Rev. A* **57**, R701 (1998).
- [4] W. A. Bryan, J. H. Sanderson, A. El-Zein, W. R. Newell, P. F. Taday, and A. J. Langley, *J. Phys. B: At. Mol. Opt. Phys.* **33**, 745 (2000).
- [5] A. Hishikawa, A. Hasegawa, and K. Yamanouchi, *Chem. Phys. Lett.* **61**, 245 (2002).
- [6] J. H. Sanderson, A. El-Zein, W. A. Bryan, W. R. Newell, A. J. Langley, and P. F. Taday, *Phys. Rev. A* **59**, R2567 (1999).
- [7] J. H. Sanderson, T. R. J. Goodworth, A. El-Zein, W. A. Bryan, W. R. Newell, A. J. Langley, and P. F. Taday, *Phys. Rev. A* **65**, 043403 (2002).
- [8] J. H. Sanderson, R. V. Thomas, W. A. Bryan, W. R. Newell, A. J. Langley, and P. F. Taday, *J. Phys. B: At. Mol. Opt. Phys.* **31**, L599 (1998).
- [9] A. Hishikawa, A. Iwamae, and K. Yamanouchi, *Phys. Rev. Lett.* **83**, 1127 (1999).
- [10] A. Hishikawa, A. Iwamae, K. Hoshina, M. Kono, and K. Yamanouchi, *Chem. Phys. Lett.* **282**, 283 (1998).
- [11] A. Hishikawa, A. Iwamae, and K. Yamanouchi, *J. Chem. Phys.* **111**, 8871 (1999).
- [12] L. J. Frasinski, P. A. Hatherly, K. Codling, M. Larsson, A. Persson, and C. G. Wahlstrom, *J. Phys. B: At. Mol. Opt. Phys.* **27**, L109 (1994).
- [13] C. Cornaggia, M. Schmidt, and D. Normand, *J. Phys. B: At. Mol. Opt. Phys.* **27**, L123 (1994).
- [14] C. Cornaggia, *Phys. Rev. A* **54**, R2555 (1996).
- [15] P. Hering and C. Cornaggia, *Phys. Rev. A* **59**, 2836 (1999).
- [16] K. Zhao, G. Zhang, and W. T. H. III, *Phys. Rev. A* **68**, 063408 (2003).
- [17] H. Hasegawa, A. Hishikawa, and K. Yamanouchi, *Chem. Phys. Lett.* **349**, 57 (2001).
- [18] F. Légaré, I. V. Litvinyuk, P. W. Dooley, F. Quéré, A. D. Bandrauk, D. M. Villeneuve, and P. B. Corkum, *Phys. Rev. Lett.* **91** (2003).
- [19] F. Légaré, K. Lee, I. V. Litvinyuk, P. W. Dooley, A. D. Bandrauk, D. M. Villeneuve, and P. B. Corkum, *Phys. Rev. Lett.* **72**, 052717 (2005).
- [20] A. Hishikawa, M. Ueyama, and K. Yamanouchi, *J. Chem. Phys.* **122**, 151104 (2005).
- [21] A. Hishikawa, H. Hasegawa, and K. Yamanouchi, *Chem. Phys. Lett.* **361**, 245 (2002).
- [22] M. Ueyama, H. Hasegawa, A. Hishikawa, and K. Yamanouchi, *J. Chem. Phys.* **122**, 154305 (2005).
- [23] T. Zuo and A. D. Bandrauk, *Phys. Rev. A* **52**, 2511 (1995).
- [24] T. Seideman, M. Y. Ivanov, and P. B. Corkum, *Phys. Rev. Lett.* **75**, 2819 (1995).
- [25] J. H. Posthumus, A. J. Giles, M. R. Thompson, and K. Codling, *J. Phys. B: At. Mol. Opt. Phys.* **29**, 5811 (1996).
- [26] H. Kono, S. Koseki, M. Shiota, and Y. Fujimura, *J. Phys. Chem.* **105**, 5627 (2001).
- [27] M. Brewczyk, K. Rzazewski, and C. W. Clark, *Phys. Rev. Lett.* **78**, 191 (1997).
- [28] P. Hering, M. Brewczyk, and C. Cornaggia, *Phys. Rev. Lett.* **85**, 2288 (2000).
- [29] M. Lezius, V. Blanchet, M. Y. Ivanov, and A. Stolow, *J. Chem. Phys.* **117**, 1575 (2002).
- [30] I. Kawata, H. Kono, and A. D. Bandrauk, *Phys. Rev. A* **64**, 043411 (2001).
- [31] J. P. Nibarger, S. V. Menon, and G. N. Gibson, *Phys. Rev. A* **63**, 053406 (2001).
- [32] S. V. Menon, J. P. Nibarger, and G. N. Gibson, *J. Phys.*

- Rev. A. **35**, 2961 (2002).
- [33] R. N. Coffee and G. N. Gibson, Phys. Rev. A. **72**, 011401 (2005).
- [34] R. N. Coffee and G. N. Gibson, Phys. Rev. A. **69**, 053407 (2004).
- [35] L. Quaglia and C. Cornaggia, Phys. Rev. Lett. **84**, 4565 (2000).
- [36] C. Cornaggia and P. Hering, Phys. Rev. A. **62**, 023403 (2000).
- [37] L. J. Frasinski, K. Codling, and P. A. Hatherly, Science **246**, 973 (1989).
- [38] D. Strickland and G. Mourou, Opt. Commun. **56**, 219 (1985).
- [39] W. C. Wiley and I. H. McLaren, Rev. Sci. Instrum. **26**, 1150 (1955).
- [40] L. J. Frasinski, P. A. Hatherly, and K. Codling, Phys. Lett. A **156**, 227 (1991).
- [41] S. Morse, M. Takahashi, J. H. D. Eland, and L. Karlsson, Int. J. Mass. Spectrom. **184**, 67 (1999).
- [42] R. Feng, G. Cooper, Y. Sakai, and C. E. Brion, Chem. Phys. **255**, 353 (2000).
- [43] P. Wang and C. R. Vidal, J. Chem. Phys. **118**, 5383 (2003).
- [44] J. S. Wright, G. A. DiLabio, D. R. Matusek, P. B. Corkum, M. Y. Ivanov, C. Ellert, R. J. Buenker, A. B. Alekseyev, and G. Hirsch, Phys. Rev. A. **59**, 4512 (1991).
- [45] J. B. Greenwood, I. M. G. Johnstone, P. McKenna, I. D. Williams, T. R. J. Goodworth, J. H. Snaderson, W. A. Bryan, A. E.-Z. adn W. R. Newell, A. J. Langley, and E. J. Divall, Phys. Rev. Lett. **88**, 233001 (2002).
- [46] T. Suzuki, H. Katayanagi, S. Nanbu, and M. Aoyagi, J. Chem. Phys. **109**, 5778 (1998).